WARSAW UNIVERSITY OF TECHNOLOGY Index 351733
FACULTY OF CIVIL ENGINEERING
COMMITTEE FOR CIVIL AND WATER ENGINEERING
POLISH ACADEMY OF SCIENCES ISSN 1230-2945

DOI: 10.24425/ace.2026.1332

ARCHIVES OF CIVIL ENGINEERING

Vol. LXXII ISSUE 3 2026

pp. 35–50



**Research paper**

# Comprehensive analysis of the temperature stress of the ice sheet in a prefabricated curling ice rink

**Junxing Li[1,2]**

**Abstract:** Prefabricated ice rinks represent a novel category of artificial ice rinks that exhibit significant potential due to low refrigeration energy consumption, multifunctional capabilities, and ease of assembly. Given the ice's considerable thickness and significant temperature gradient, it is imperative to investigate the temperature-induced stresses. Three temperature models of the prefabricated rink, considering the actual thermal environment, were established based on the theory of heat transfer. Employing the sequential coupled analysis method, a refined model for analyzing temperature stress within the ice was established. A method for applying temperature to un-refined ice sheet was proposed, utilizing the mathematical functions derived from temperature distribution results. The distribution characteristics of temperature stress fields and the influence of various heat exchange processes were examined. Additionally, the effects of different thermal environment factors on temperature stress were analyzed, and parameters sensitivities were determined. The results show that honeycomb supports are not suitable for embedding constraints analogous to reinforced concrete. The critical temperature-induced tensile stress occurs beneath cooling tubes interfacing with ice, with its magnitude showing positive correlation with refrigerant-driven ice temperature reduction. In contrast, reducing ice temperature through thermal convection and radiation results in a decrease in tensile stress. Parameter analysis reveals that refrigerant constitutes the principal governing factor for temperature stress development. This study would contribute to the performance analysis of ice rinks under thermal-mechanical coupling effects.

**Keywords:** prefabricated ice rink, ice sheet, temperature field, temperature stress, finite element modelling, distribution characteristic

[1]Assoc. Prof., PhD., Eng., Nanyang Normal University, School of Civil Engineering and Architecture, Nanyang 473061, China, e-mail: 20231076@nynu.edu.cn, ORCID: 0009-0008-7512-3968

[2]PhD., Eng., Harbin Institute of Technology, School of Civil Engineering, Harbin 150090, China, e-mail: 20231076@nynu.edu.cn, ORCID: 0009-0008-7512-3968

# 1. Introduction

With the growing public interest in ice sports, China has achieved substantial advancements in ice rink infrastructure development [1–4]. Traditional rinks, such as the National Speed Skating Hall in Beijing, serve as permanent facilities for international- level ice competitions [5]. In contrast, movable ice rinks demonstrate flexibility and economic efficiency through modular disassembly and spatial adaptability. For instance, the National Aquatics Center, has achieved the efficient swimming pool-to-rink conversion through a detachable, modular system [6]. However, prefabricated ice rinks encounter several challenges in practical applications, including non-uniform temperature gradients and induced temperature stress within ice sheets.

Ice exhibits distinct thermomechanical behavior characterized by a linear thermal expansion coefficient approximately five times that of conventional construction materials like steel and concrete. This characteristic induces significant temperature stress fields due to temperature fluctuations, necessitating differentiated engineering focuses for expansion [7, 8] versus contraction [9, 10] scenarios.

The existing studies mainly focus on dams and reservoirs, providing valuable insights into the behavior of ice under temperature stress [11–13]. Cox [14] utilized a self-made bidirectional stress sensor to measure the expansion load exerted by lake ice on the shore. Carter [15] measured the temperature stress of reservoir ice. Petrich [16] explored the spatial and temporal distribution of the thermal expansion load, revealing that the temperature stress field of ice was unevenly distributed due to incomplete boundary restrictions. Marchenko [17] observed the temperature expansion load of 2-meter-thick sea ice on the steel structure support of a coal wharf in situ. Hellgren [18, 19] designed and optimized a device for measuring static ice loads, which captures the temperature expansion and shrinkage load across the entire ice thickness. In terms of theoretical and finite element analysis, Bažant [20] analyzed the bending fracture of a floating ice sheet caused by temperature stress using plate bending theory. Goldstein [21] employed an asymptotic approach to study the brittle fracture of a freshwater ice sheet under thermal shock. Kharik [22] employed the finite element method to simulate the static load on a dam due to thermal expansion of ice, revealing that the initial stress within the ice exerts a limited influence on temperature stress.

In summary, temperature stresses within ice are influenced by the temperature distribution and confinement conditions. The structure of the prefabricated ice rink is distinct from that of traditional ice rinks, characterized by its ice thickness and the incorporation of refrigeration system [6]. Additionally, there is a noticeable temperature gradient. Investigating the temperature stress field of the ice sheet in prefabricated ice rinks is therefore crucial.

This paper presents an investigation into the temperature stress within a prefabricated curling rink. An overview of the prefabricated curling rink and an analysis of heat exchange processes were preliminarily presented. Meanwhile, methodologies for finite element modeling of temperature and temperature stress field were established utilizing ABAQUS. Furthermore, the effect of various parameters on the temperature stress was investigated.

# 2. Description and heat exchange of the prefabricated ice rink

The prefabricated curling rink for the 2022 Beijing Winter Olympic Games comprises: the basic conversion structure, functional layer, and ice sheet structure. The ice sheet structure includes the ice, corrugated cooling tubes, and honeycomb-shaped cooling tube supports. More detailed information of the structural diagrams of the prefabricated rink can be found in [6].

Figure 1 depicts the heat transfer processes that occur between the ice and the surrounding enlivenment. The total thermal load on the ice sheet can be articulated as follows [10]:

$$Q = Q_{\text{conv}} + Q_{\text{mass}} + Q_{\text{lrad}} + Q_{\text{srad}} \tag{2.1}$$

where $Q_{\text{conv}}$, $Q_{\text{mass}}$, $Q_{\text{lrad}}$, and $Q_{\text{srad}}$ are convective heat transfer, mass heat transfer, long-wave radiative heat transfer and short-wave radiative heat transfer, respectively.

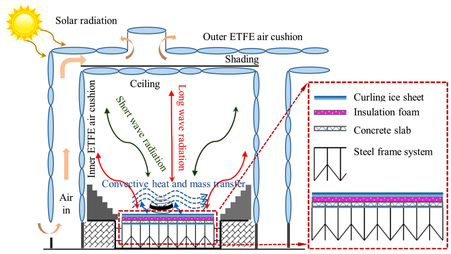

Fig. 1. Schematic of ice sheet heat transfer

The heat flow density of convective heat transfer can be determined as follows:

$$Q_{\text{conv}} = h_c(T_{\text{closest}} - T_{\text{ice}}) \tag{2.2}$$

where $T_{\text{closest}}$ is surrounding air temperature, $T_{\text{ice}}$ is ice surface temperature, $h_c$ is the convective heat transfer coefficient.

The density of heat flow during mass transfer can be calculated as:

$$Q_{\text{mass}} = h_m(d_{\text{closest}} - d_{\text{ice}})r \tag{2.3}$$

where $d_{\text{closest}}$ and $d_{\text{ice}}$ are the humidity ratio and saturated humidity ratio of the air; $r$ is the latent heat of the water-ice phase transition; $h_m$ is the convective mass transfer coefficient.

The long-wave radiation fluxes can be calculated as:

$$Q_{\text{lrad}} = \sum_{i=1}^{N} \varepsilon_i \sigma T_i^4 F_{i-s} - \varepsilon_s \sigma T_s^4 \tag{2.4}$$

where $\varepsilon_i$ and $\varepsilon_s$ are the emissivity of the ceiling/wall and the ice surface; $T_i$ and $T_s$ are the temperature of the ceiling/wall and the ice surface; $F_{i-s}$ is the view factor from the ice surface to ceiling/wall surface; $\sigma$ is the Stefan–Boltzmann constant.

# 3. Simulation of the ice temperature distribution

## 3.1. Simulation method of ice temperature

Three categories of finite element models for the temperature field have been developed using ABAQUS. Simplified model A disregards the honeycomb support, while simplified model B adapts reinforced concrete modeling technique and constrains the honeycomb support by embedding it within the ice [23–25]. Finally, refined model C places the honeycomb support in contact with the surrounding ice.

The expressions for thermal conductivity (W/m ·° C), specific heat capacity (kJ/kg ·° C), and density (kg/m$^3$) are presented as [26]:

$$k = 1.16\left(1.91 - 8.66 \times 10^{-3}T + 2.97 \times 10^{-5}T^2\right), \quad -173°\text{C} < T < 0°\text{C} \tag{3.1}$$

$$C = 2.067 + 6.89 \times 10^{-3}T, \quad -183°\text{C} < T < 0°\text{C} \tag{3.2}$$

$$\rho = 917\left(1 - 1.17 \times 10^{-4}T\right), \quad -140°\text{C} < T < 0°\text{C} \tag{3.3}$$

The ABAQUS/Standard module is selected to conduct a steady-state analysis of the initial temperature state. Following this, a transient analysis is conducted to simulate the temperature evolution of the ice sheet. The DC3D8 has been selected for the discretization of each component within the model. The mesh sizes of the cooling tubes and honeycomb supports are 3 mm and 5 mm, respectively. Within the refinement region of the ice sheet, the upper, middle, and bottom parts are meshed with sizes of 10 mm, 5 mm, and 3 mm, respectively. The thermal resistance coefficient at the ice-cooling tube interface was adopted as 0.0005 m$^2$ · K/W, half of the steel-concrete interface [27]. To simplify the simulation, temperature boundary conditions were applied directly to the inner wall of the cooling tubes.

## 3.2. Verification and distribution of the temperature field within the ice

Figure 2a presents the temperature variations at different depths within the ice sheet, as derived from measurements [10] and modeling. The temperature distributions predicted by the FEM closely match the experimental outcomes, indicating a high level of agreement between the two datasets. Fig. 2b provides a comparative analysis of the temperature variations derived from the three models. The temperature curves exhibit a high degree of consistency.

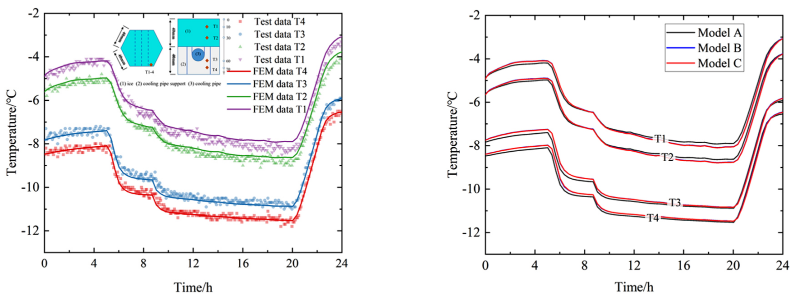


(a) (b)

Fig. 2. Comparison of ice temperature: (a) re efined model l C, (b) three e models

Figure 3a illustrates the temperature distribution across the thickness of the ice sheet, which follows a nonlinear pattern. With reference to [28], polynomial functions were employed to describe the temperature distribution. Fig. 3b displays the sinusoidal distribution of the ice temperature in the horizontal direction, with the lowest temperatures occurring above the cooling tubes and the highest above the spaces between them.

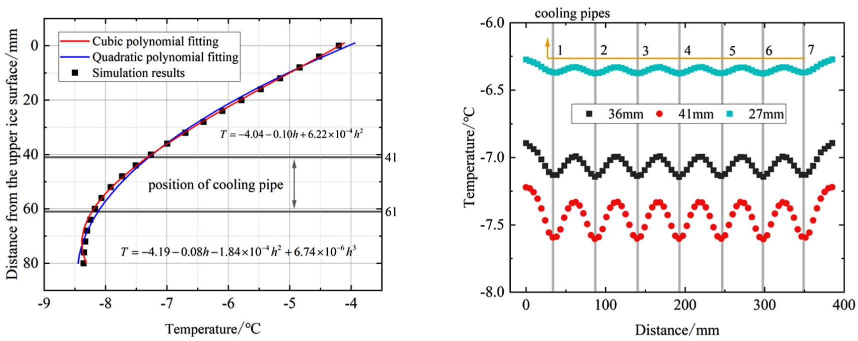


(a) (b)

Fig. 3. Temperature distribution of ice sheet: (a) thickness direction, (b) horizontal direction

# 4. Theoretical formula on temperature stress of ice sheet

Westergaard [29] derived the analytical solution for the temperature stress in a concrete slab under the influence of a linear temperature gradient. In the calculation of warping stresses, several assumptions were made: the plate was considered isotropic and elastic, the self-weight was neglected, and Winkler foundation was always in contact with the slab. The deflection $\omega$ of a finite-size plate of dimensions $A \times B$ can be decomposed as [30]:

$$\omega(x, y) = \omega(x) + \omega(y) \tag{4.1}$$

where $\omega(x)$ is the deflection of the plate with finite size $A$ in one direction and infinite size in the other direction; $\omega(y)$ is the deflection of the plate with finite size $B$ in one direction and infinite size in the other direction. The maximum warping stress in the plate is:

$$\sigma_x = \frac{E\alpha_t \Delta T}{2(1-\mu^2)}\left(C_x + \mu C_y\right) \tag{4.2}$$

$$\sigma_y = \frac{E\alpha_t \Delta T}{2(1-\mu^2)}\left(\mu C_x + C_y\right) \tag{4.3}$$

where $E$ and $\alpha_t$ are the elastic modulus and linear expansion coefficient of ice, both of which are temperature related parameters; $C_x$ and $C_y$ are W–B warping stress coefficients, which are calculated as:

$$C_x = 1 - \frac{2\cos\vartheta_A \cosh\vartheta_A}{\sin 2\vartheta_A + \sinh 2\vartheta_A}\left(\tan\vartheta_A + \tanh\vartheta_A\right) \tag{4.4}$$

$$C_y = 1 - \frac{2\cos\vartheta_B \cosh\vartheta_B}{\sin 2\vartheta_B + \sinh 2\vartheta_B}\left(\tan\vartheta_B + \tanh\vartheta_B\right) \tag{4.5}$$

$$\vartheta_A = \frac{A}{2\sqrt{2}l}, \quad \vartheta_B = \frac{B}{2\sqrt{2}l}, \quad l = \sqrt[4]{\frac{Eh^3}{12(1-\mu^2)k}} \tag{4.6}$$

Considering that the actual ice sheet structure, the W–B warping stress calculation formula cannot be directly applied to the ice sheet. However, the presented formula can offer valuable qualitative insights for assessing temperature stress.

# 5. FEM of ice temperature stress in prefabricated rink

## 5.1. Finite element simulation method of ice temperature stress

### 5.1.1. Simulation process of ice temperature stress field

As shown in Fig. 4, a refined temperature stress field model was developed for the prefabricated rink. Consistent with temperature modeling method, the temperature stress analysis incorporates three modeling approaches: model A, model B, and refined model C. The sequentially coupled thermal-stress method, solving temperature stress based on the existing temperature field, was selected. As illustrated in Fig. 5, a heat transfer analysis is initially conducted to ascertain the temperature distribution. Following this, the thermal results are transferred to the static analysis step as the predefined temperature field. Ultimately, the temperature stress results are computed through applying boundary condition constraints and thermal expansion effects.

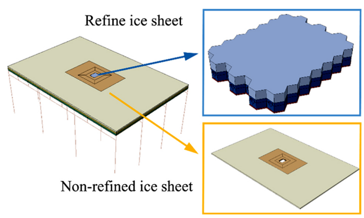

Fig. 4. FEM model of temperature stress

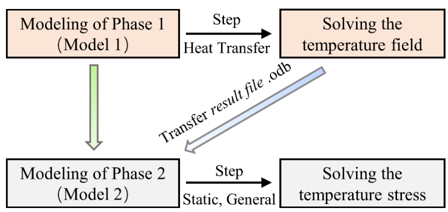

Fig. 5. Analysis method of temperature stress

The ice employs a thermoelastic constitutive model. The temperature-dependent elastic modulus is derived from [31]. The coefficient of linear thermal expansion of ice can be determined as [27]:

$$\alpha_t = 0.33\,(0.67T + 158.16) \times 10^{-6} \tag{5.1}$$

The cooling tubes and honeycomb supports were characterized using elastic-plastic constitutive models. The constitutive relationship of steel, concrete and XPS are based on methodologies in [6]. The interactions between the ice-cooling tube, ice-honeycomb support, and cooling tube-honeycomb support were defined by Tie constraints. The contact relationship between other components was the same with our previous studies [6].

### 5.1.2. Temperature application method for the non-refined region ice sheet

The non-refined region temperature was determined by temperature functions. Based on the temperature distribution characteristics, the temperature function consists of a polynomial function describing the temperature gradient through the ice thickness and a variable amplitude sinusoidal function representing horizontal temperature variations.

$$T(x, y) = T_0(y) + A(y)\sin\left(2\pi\frac{x - x_0}{x_d}\right) \tag{5.2}$$

$$T_0(y) = \sum_{i=0}^{5} a_i y^i \tag{5.3}$$

$$A(y) = b + c\exp\left[-2\left(\frac{y-d}{e}\right)^2\right] \tag{5.4}$$

where $a \sim e$ are the fitting parameters of the temperature distribution functions; $x_0$ is the coordinate of the ice surface center on the $x$ axis, and $x_d$ is the spacing of the cooling tubes; $T_0$ represents the temperature distribution in the thickness direction, and $A$ represents the amplitude of the sinusoidal distribution of ice temperature in the horizontal direction. This parameter is related to the position in thickness direction (i.e., $y$ axis) and follows a Gaussian distribution.

## 5.2. Verification of finite element results of temperature stress

Using a homogeneous ice plate (elastic modulus of 700 MPa) with a linear temperature gradient (top: –5°C, bottom: –15°C) as a case study. As displayed in Fig. 6, the ice experiences bending deformation with tensile stress at the bottom surface and compressive stress at the top surface. The stress distribution patterns in horizontal directions are consistent between model A and refined model C. Through-thickness direction (S22) in model A reveals tension above and below cooling tubes and lateral compression. Simplified model B exhibits uniform tensile stress (~0.1 MPa) on the ice surface above honeycomb supports, significantly exceeding stress magnitudes observed in the other two models.

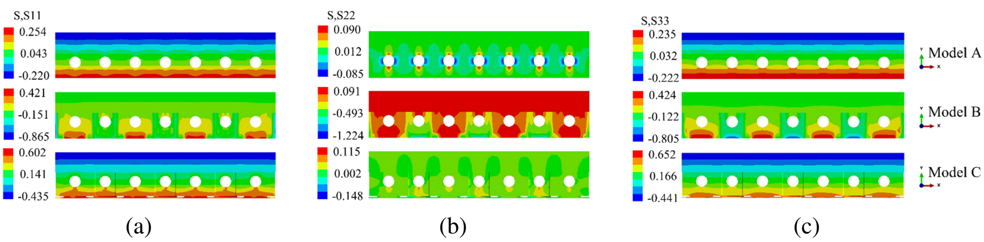


Fig. 6. Normal stress distribution of ice sheet: (a) S11, (b) S22, (c) S33

Figure 7 presents the principal stresses. The stress contours of model A and refined model C are similar, featuring compressive states on the upper surface and tensile states on the lower surface. Simplified model B, however, shows alternating tensile/compressive states along the bottom surface. Fig. 8 shows a comparison of the theoretical temperature stress with finite element model results under a linear temperature gradient. Simplified model A closely matches the theoretical values, confirming minimal impact of cooling tube perforations on temperature stress. However, both honeycomb support-integrated models exhibit elevated stress levels, indicating significant ice-support interaction effects.

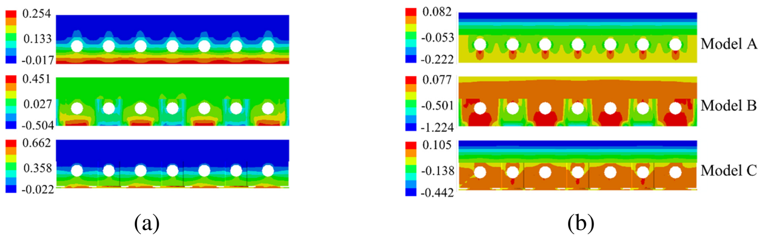


Fig. 7. Principal stress: (a) maximum, (b) minimum

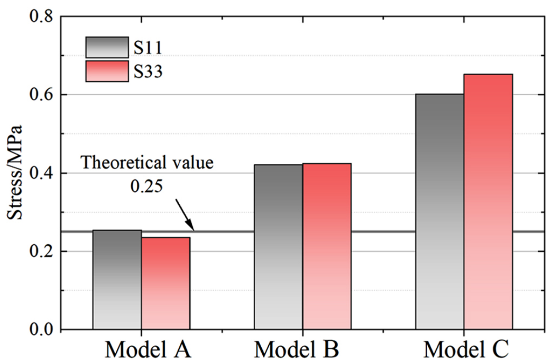


Fig. 8. Comparison of results

## 5.3. Distribution characteristics of initial temperature stress

Figure 9a illustrates the stress field of simplified model A, wherein tensile band (S11) is formed between the cooling tubes beneath the ice. Through-thickness stress (S22) showing tensile zones above/below cooling tubes with lateral compression. Fig. 9b presents the temperature stress distribution of model B. The stress on the bottom surface exhibits alternating tension and compression. This pattern may arise from the 2 mm ice sheet beneath honeycomb supports being insufficient to provide the restraining effect as the protective layer on the steel bar within a reinforced concrete structure. Therefore, the embedded contact simulation method, is not appropriate for the ice sheet. Fig. 9c shows the temperature stress of refined model C. Similar to the simplified model A, the ice below the cooling tube is subjected to tension in horizontal directions. The normal stress in thickness direction (S22) results in slight tensile states in peritubular upper/lower ice regions.

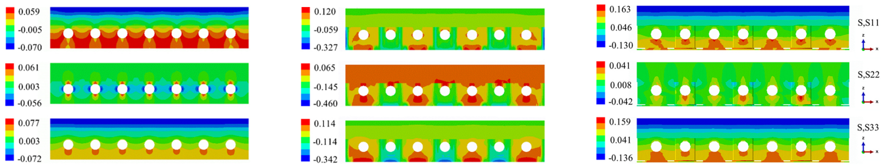

(a) (b) (c)

Fig. 9. Temperature stress distribution: (a) model A, (b) model B, (c) refined model C

In summary, while the simplified model effectively captures temperature distribution, its exclusion of critical components renders it insufficient for temperature stress analysis. In fact, temperature stresses are progressively relieved through multiple phase-change freezing processes. Therefore, the present work primarily focuses on temperature stress variations.

# 6. Variation characteristics of temperature stress

## 6.1. Temperature stress driven by refrigerant temperature change

Figure 10a depicts the most unfavorable temperature stress beneath the cooling tube during cooling. The heat exchange parameters were as follows: radiation boundary at 20°C, convective air temperature of 10°C (velocity: 0.2 m/s), and ethylene glycol solution temperature reduction from –14.2°C to –19.2°C within 10 minutes. The temperature stress increased progressively during cooling phase, reaching maximum magnitude approximately 10 minutes post-cooling termination due to thermal inertia. Subsequent stress relaxation occurred through gradual thermal equilibration. Furthermore, it is observable that the variation trend of temperature stress aligns with that of its maximum temperature difference. Under refrigerant temperature increase scenarios, Fig. 10b illustrates temperature tensile stress evolution during ice warming process. Ethylene glycol temperature uniformly increases to –9.2°C under constant environmental conditions. Contrary to the cooling-induced temperature stress, the stress decreases gradually as the ice temperature increases, and then gradually increases. The variation trend of the temperature stress is consistent with maximum thermal gradient within the ice sheet.

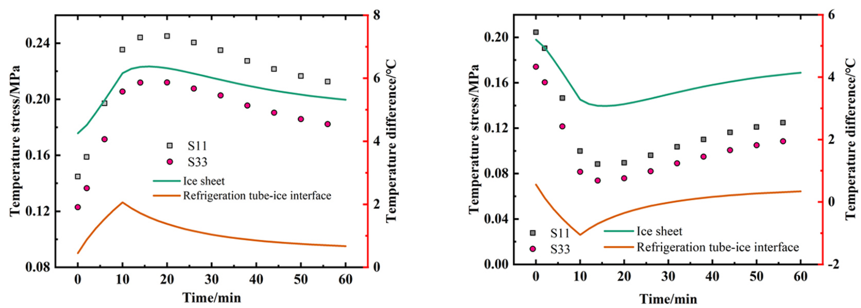


(a) (b)

Fig. 10. Temperature stress driven by refrigerant temperature (a) decreases and (b) increases

## 6.2. Temperature stress driven by convective temperature change

Under simulated conditions with an initial air temperature of 10°C (reduced to 5°C over 10 minutes), constant air velocity (0.2 m/s), radiative temperature (20°C), and ethylene glycol temperature (–14.2°C), Fig. 11a presents critical temperature stress and temperature difference. Contrary to refrigerant-driven cooling scenarios, the stress decreases as temperature decreases. Unlike the cooling medium lowering the ice temperature primarily through heat conduction, heat convection results in a slow ice temperature change. Fig. 11b illustrates the evolution of temperature stress during the air temperature increasing 5°C. In contrast to the cooling process described above, the temperature stress gradually increases with increasing ice temperature before stabilizing at a relatively constant level.

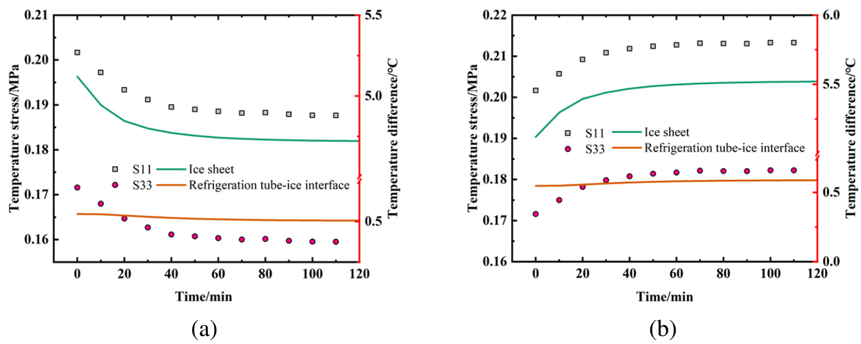


Fig. 11. Temperature stress driven by convective air temperature (a) decreases and (b) increases

## 6.3. Temperature stress driven by radiation temperature change

Initial radiation temperature of 20°C decreased to 15°C after 10 minutes. Other parameters remained constant: 10°C air temperature, 0.2 m/s air velocity, and –14.2°C glycol solution temperature. As depicted in Fig. 12a, the stress decreases with ice temperature reduction, reaching minimum values 40 minutes post-cooling termination. Fig. 12b demonstrates radiation-driven temperature stress evolution for ice warming. Initial radiation temperature was 20°C, decreasing to 15°C. Contrary to the cooling process, temperature stress gradually increases with rising ice temperature, and then remains basically unchanged.

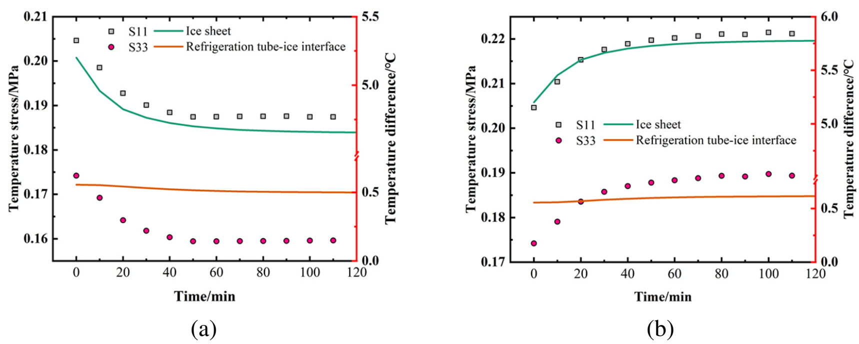


Fig. 12. Temperature stress driven by radiation temperature (a) decreases and (b) increases

In summary, temperature-induced stress evolution is not consistent with ice temperature variations due to distinct heat transfer mechanisms. Refrigerant-driven ice cooling results in an increase in temperature stress, whereas cooling ice driven by convection and radiation leads to a decrease in temperature stress. Considering its significant compressive strength but limited tensile resistance [31, 32], this section focuses on the temperature-induced tensile stress.

## 6.4. Analysis of influencing factors on temperature stress

### 6.4.1. Influences of refrigerant related factors

Figure 13a demonstrates maximum tensile stress evolution under three refrigerant initialization conditions: –8°C, –14°C, and –20°C, with 5°C reduction. Tensile stress magnitude exhibits positive correlation with initial temperature decreases. This aligns with the temperature stress theory of that temperature stress increases as the elastic modulus increases. Fig. 13b shows the variation of maximum tensile stress when the refrigerant decreases by 5°C at different rates. The decreasing rate has minimal impact on tensile stress magnitude. Fig. 13c examines cooling amplitude impacts from –8°C baseline with 5°C, 10°C, and 15°C reductions. The stress magnitude increases with the decreasing amplitude of the refrigerant fluid, increasing about 2.1 times when the amplitude increases from 5°C to 15°C. In short, the stress is closely related to the initial temperature and cooling amplitude of refrigerant fluid, whereas demonstrates negligible sensitivity to the cooling rate.

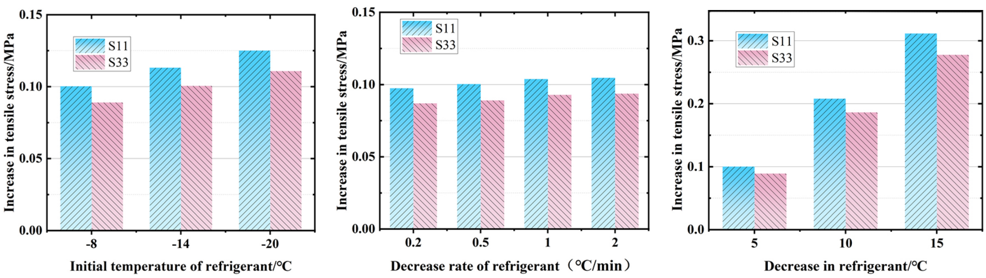


(a) (b) (c)

Fig. 13. Influences of refrigerant factors: (a) initial temperature, (b) cooling rate, (c) temperature drop

### 6.4.2. Influence of convection-related factors

Figure 14a demonstrates maximum tensile stress evolution under convective air temperature rises of 5°C, 10°C, and 15°C. The tensile stress generated in the ice sheet shows positive correlation with the magnitude of air temperature increasing. Fig. 14b shows the changes in tensile stress for air velocity with 0.5 m/s, 1.0 m/s, and 1.5 m/s increments. The tensile stress increases with the convective air velocity. In summary, elevations in both air temperature and velocity amplify tensile stress within the ice sheet.

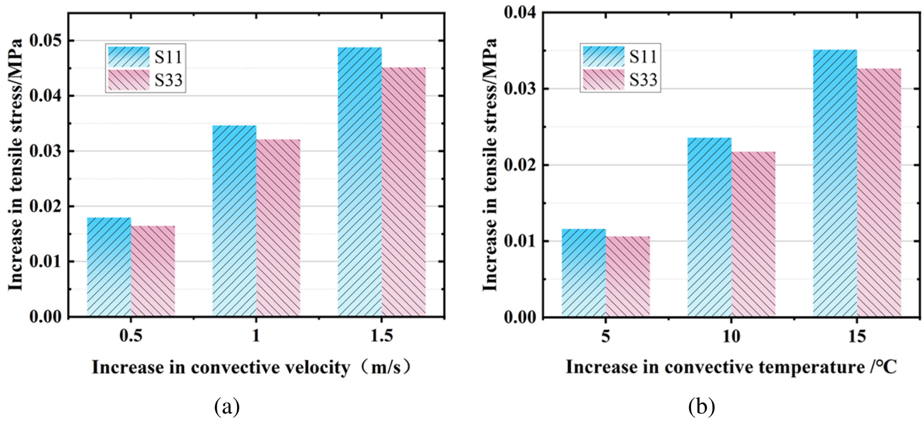


Fig. 14. Influence of convection-related factors: (a) air temperature, (b) air velocity

#### 6.4.3. Influence of radiation-related factors

Figure 15a shows the variation in tensile stress under initial radiation temperatures of 10°C, 20°C, and 30°C. The stress exhibits a slight increase with higher initial radiation temperatures. As radiation temperature rises from 10°C to 30°C, the tensile stress exhibits an approximate 15% increase. Fig. 15b illustrates the tensile stress when the radiation temperature increased by 5°C, 10°C, and 15°C, respectively. The stress is positively correlated with the radiation amplitude. An elevation in radiation temperature enhances heat exchange between the ice surface and the surrounding environment, leading to a more pronounced temperature gradient. Radiation heating amplitude demonstrates greater influence on temperature tensile stress development than initial radiation temperature parameters.

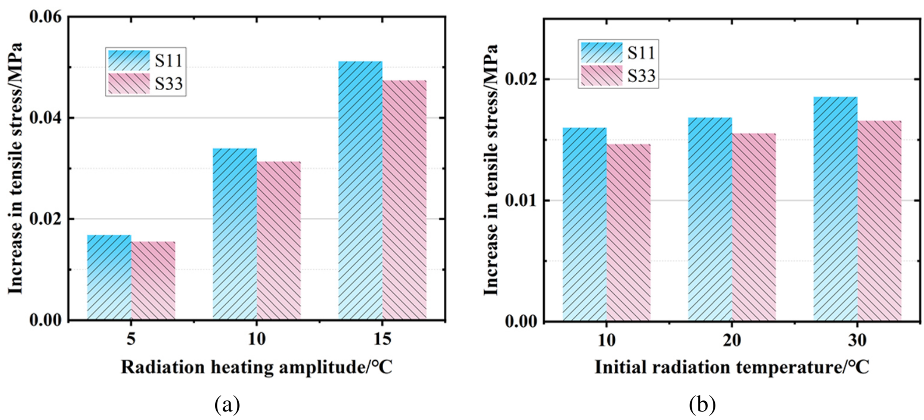


Fig. 15. Influence of radiation-related factors: a) initial temperature, (b) heting amplitude

#### 6.4.4. Influence of ice constraint conditions

Figure 16 demonstrates boundary constraint effects on tensile stress development. The higher the degree of constraint, the greater the tensile stress generated. The stress under consolidation constraint is 0.41 MPa, approximately half of its tensile strength. Therefore, a flexible enclosure structure or a certain gap between ice and enclosure can be beneficial.

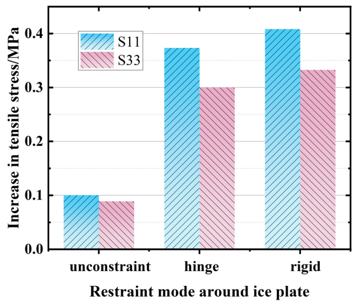


Fig. 16. Influence of constraint conditions

#### 6.4.5. Comparison of influencing factors on temperature stress

To compare the impact of various heat exchange factors, a dimensionless temperature stress sensitivity coefficient is defined as:

$$\eta_s = \frac{\Delta S/S_0}{\Delta X/X_0} \times 100\% \tag{6.1}$$

where $\eta_s$ is the stress sensitivity, $\Delta S$ and $S_0$ are the temperature stress and unit stress, $\Delta X$ and $X_0$ are the change in influencing factors and unit influencing factors, respectively.

Figure 17 illustrates the degree of various heat exchange factors on the temperature stress. Refrigerant cooling magnitude and the air flow velocity significantly impact the temperature tensile stress. It should be noted that unlike outdoor ice rinks, indoor ice rinks exhibit stable airflow characteristics and negligible variations in air velocity. The environmental parameters related to thermal convection and thermal radiation have little effect on temperature stress. These observations are consistent with the analysis of factors impacting ice temperature.

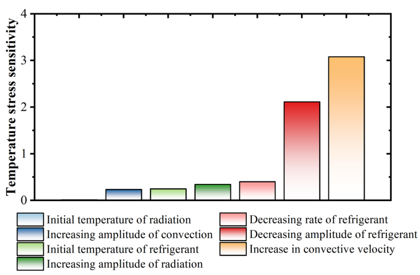


Fig. 17. Comparison of influencing factors

# 7. Conclusions

1. Three models for ice temperature-stress analysis were established, incorporating a temperature mapping method for non-refined areas. The simplified model neglecting honeycomb supports results in minimal temperature stress. The constraint analogy with reinforced concrete proves not suitable for honeycomb supports. Stress distributions exhibit compressive dominance in upper ice sheets and tensile states at lower parts, with critical tensile stress occurring at the ice-cooling tube interface.
2. The characteristics of temperature stress within the ice sheet were obtained by simulating thermal expansion and contraction. Temperature stress typically corresponds with thermal gradient variations rather than absolute temperature changes. When ice cooling is driven by the refrigerant, there is an increase in temperature tensile stress. In contrast, when cooling is attributed to heat convection and heat radiation, the stress tends to decrease.
3. Through parameter analysis, the influence of various factors on the temperature tensile stress was determined. The stress is minimally affected by the initial temperature, temperature increase rate, and temperature increase amplitude associated with heat convection and heat radiation. Whereas the decreased amplitude of the cooling liquid and surface air velocity exhibit notable impacts on the temperature tensile stress.

Finally, due to limitations in instrumentation accessibility and the construction process of prefabricated rink, in-situ stress measurements were not included. In future work, strain sensors and small force sensors, overcoming temperature and space effects, will be embedded within the ice sheet to strengthen the understanding of temperature stress.

# Acknowledgements

The author gratefully acknowledges the financial support by Natural Science Foundation of Henan Province (252300420490), and the National Natural Science Incubation Project of Nanyang Normal University (2025PY012).

## References

[1] L. Li, X. Liu, and T. Zhang, “Investigation of heat and mass transfer characteristics in the ice rink: Ice making, maintaining and resurfacing processes”, *Building and Environment*, vol. 196, art. no. 107779, 2021, doi: 10.1016/j.buildenv.2021.107779.

[2] W. Lin, X. Liu, S. Li, and T. Zhang, “Investigation on thermal environment and heat transfer characteristics in ice rinks with different envelopes”, *Building and Environment*, vol. 219, art. no. 109250, 2022, doi: 10.1016/j.buildenv.2022.109250.

[3] Y. Yang, J. Li, W. Zhang, and F. Zheng, “Research on the contribution rate of photovoltaic power in indoor ice arenas across different climatic zones: A case study in China”, *Energy and Built Environment*, vol. 7, no. 1, pp. 28–40, 2024, doi: 10.1016/j.enbenv.2024.09.001.

[4] W. Lin, X. Liu, T. Zhang, and X. Liu, “Entransy analysis and performance optimization of the heat and humidity removal process in artificial ice rinks”, *Journal of Building Engineering*, vol. 86, art. no. 108896, 2024, doi: 10.1016/j.jobe.2024.108896.

[5] S. Lu, H. Qian, Q. Guo, and M. Gu, “Energy-saving performance and mechanism studies on membrane ceiling: A case study of the National Speed Skating Oval”, *Energy for Sustainable Development*, vol. 72, pp. 88–99, 2023, doi: 10.1016/j.esd.2022.11.004.

[6] W. Zhang, J. Li, Q. Yang, and L. Mu, "Practical application of a novel prefabricated curling ice rink supported by steel-concrete composite floors: In situ measurements of static and dynamic response", *Structures*, vol. 32, pp. 1888–1906, 2021, doi: 10.1016/j.istruc.2021.04.011.

[7] H. Han, L. Shen, M. Cao, L. Wei, and X. Qian, "On the ice induced damage of reservoir drainage tower: A thermal stress-involved contact simulation", *Engineering Failure Analysis*, vol. 160, art. no. 108203, 2024, doi: 10.1016/j.engfailanal.2024.108203.

[8] G. White and A. McCallum, "Review of ice and snow runway pavements", *International Journal of Pavement Research and Technology*, vol. 11, no. 3, pp. 311–320, 2018, doi: 10.1016/j.ijprt.2017.11.002.

[9] D.M. Masterson, "State of the art of ice bearing capacity and ice construction", *Cold Regions Science and Technology*, vol. 58, no. 3, pp. 99–112, 2009, doi: 10.1016/j.coldregions.2009.04.002.

[10] J. Li, J. Yang, Q. Liu, J. Xu, W. Zhang, and Q. Yang, "Investigation of the temperature field of the ice sheet in a prefabricated curling ice rink: Experiment and finite element simulation", *Applied Thermal Engineering*, vol. 251, art. no. 123636, 2024, doi: 10.1016/j.applthermaleng.2024.123636.

[11] X. Deng, et al., "Static ice pressure measuring system based on fiber loop ring-down spectroscopy and FPGA", *Sensors*, vol. 20, no. 20, art. no. 5927, 2020, doi: 10.3390/s20205927.

[12] R. Hellgren and R. Malm, "Systematic literature search and meta regression of measured static ice loads on concrete dams", *Journal of Cold Regions Engineering*, vol. 38, no. 2, 2024, doi: 10.1061/JCRGEI.CRENG-661.

[13] R. Hellgren, J. Enzell, A. Ansell, E. Nordström, and R. Malm, "Estimating the ice loads on concrete dams based on their structural response", *Water*, vol. 14, no. 4, art. no. 597, 2022, doi: 10.3390/w14040597.

[14] G. Cox, "A preliminary investigation of thermal ice pressures", *Cold Regions Science and Technology*, vol. 9, no. 3, pp. 221–229, 1984, doi: 10.1016/0165-232X(84)90069-7.

[15] D. Carter, D. Sodhi, E. Stander, O. Caron, and T. Quach, "Ice Thrust in Reservoirs", *Journal of Cold Regions Engineering*, vol. 12, no. 4, pp. 169–183, 1998, doi: 10.1061/(ASCE)0887-381X(1998)12:4(169).

[16] C. Petrich, I. Sæther, L. Fransson, B. Sand, and B. Arntsen, "Time-dependent spatial distribution of thermal stresses in the ice cover of a small reservoir", *Cold Regions Science and Technology*, vol. 120, pp. 35–44, 2015, doi: 10.1016/j.coldregions.2015.09.003.

[17] A. Marchenko, "Thermo-mechanical loads of confined sea ice on structures", *Philosophical Transactions of the Royal Society A: Mathematical, Physical and Engineering Sciences*, vol. 376, no. 2129, art. no. 20170341, 2018, doi: 10.1098/rsta.2017.0341.

[18] R. Hellgren, R. Malm, L. Fransson, F. Johansson, E. Nordström, and M. Westberg Wilde, "Measurement of ice pressure on a concrete dam with a prototype ice load panel", *Cold Regions Science and Technology*, vol. 170, art. no. 102923, 2020, doi: 10.1016/j.coldregions.2019.102923.

[19] R. Hellgren, C. Petrich, B. Arntsen, and R. Malm, "Ice load measurements on Rätan concrete dam using different sensor types", *Cold Regions Science and Technology*, vol. 193, art. no. 103425, 2022, doi: 10.1016/j.coldregions.2021.103425.

[20] Z.P. Bažant, "Large-scale thermal bending fracture of sea ice plates", *Journal of Geophysical Research: Oceans*, vol. 97, no. C11, pp. 17739–17751, 1992, doi: 10.1029/92JC00816.

[21] R.V. Goldstein and N.M. Osipenko, "Fracture of ice cover under thermal stresses", *Geophysica*, vol. 42, no. 1-2, pp. 3–15, 2006.

[22] E. Kharik, B. Morse, V. Roubtsova, M. Fafard, A. Cote, and G. Comfort, "Numerical studies for a better understanding of static ice loads on dams", *Canadian Journal of Civil Engineering*, vol. 45, no. 1, pp. 18–29, 2018, doi: 10.1139/cjce-2017-0142.

[23] S. Li, H. Li, and D. Zhao, "Seismic performance of an assembled monolithic concrete column", *Archives of Civil Engineering*, vol. 70, no. 3, pp. 513–530, 2024, doi: 10.24425/ace.2024.150999.

[24] M. Cai, W. Li, Z. Wan, J. Sheng, J. Tan, and C. Ma, "Cracking control technique for continuous steel-concrete composite girders under negative bending moment", *Archives of Civil Engineering*, vol. 69, no. 3, pp. 239–251, 2023, doi: 10.24425/ace.2023.146078.

[25] S. Wang and D. Wang, "A study on the deflection and crack layout in a hollow slab bridge", *Archives of Civil Engineering*, vol. 69, no. 3, pp. 541–555, 2023, doi: 10.24425/ace.2023.146096.

[26] S. Fukusako, "Thermophysical properties of ice, snow, and sea ice", *International Journal of Thermophysics*, vol. 11, no. 2, pp. 353–372, 1990, doi: 10.1007/BF01133567.

[27] X. Peng and M. Zhou, "Thermo-mechanical behavior of composite beams with corrugated steel webs exposed to localized fire", *Journal of Constructional Steel Research*, vol. 211, art. no. 108180, 2023, doi: 10.1016/j.jcsr.2023.108180.

[28] A.R. Mohamed and W. Hansen, "Prediction of stresses in concrete pavements subjected to non-linear gradients", *Cement and Concrete Composites*, vol. 18, no. 6, pp. 381–387, 1996, doi: 10.1016/S0958-9465(96)00028-5.

[29] H.M. Westergaard, "Stresses in concrete pavements computed by theoretical analysis", *Public Roads*, vol. 7, no. 2, pp. 25–35, 1926.

[30] R.Y. Liang and Y.Z. Niu, "Temperature and curling stress in concrete pavements: analytical solutions", *Journal of Transportation Engineering*, vol. 124, no. 1, pp. 91–100, 1998, doi: 10.1061/(ASCE)0733-947X(1998)124:1(91).

[31] W. Zhang, J. Li, B. Yuan, L. Wang, and Q. Yang, "Experimental investigation of unconfined compressive properties of artificial ice as a green building material for rinks", *Buildings*, vol. 11, no. 12, art. no. 586, 2021, doi: 10.3390/buildings11120586.

[32] W. Zhang, J. Li, L. Wang, and B. Yuan, "Flexural characteristics of artificial ice in winter sports rinks: experimental study and nondestructive prediction based on surface hardness method", *Archives of Civil and Mechanical Engineering*, vol. 22, no. 1, art. no. 67, 2022, doi: 10.1007/s43452-022-00387-8.

Received: 2025-01-16, Revised: 2025-04-21